

www.acsami.org Research Article

Enhancement of Diffusion, Densification and Solid-State Reactions in Dielectric Materials Due to Interfacial Interaction of Microwave Radiation: Theory and Experiment

Abhishek Malhotra, Mahshid Hosseini, Sadeq Hooshmand Zaferani, Michael Hall, and Daryoosh Vashaee*



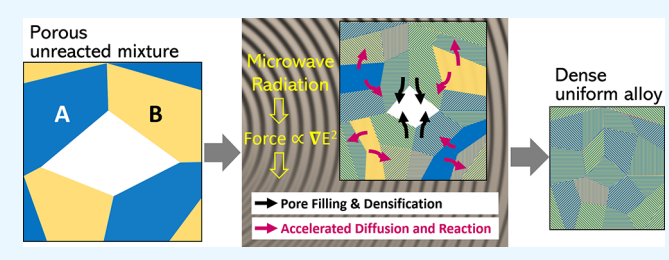
Cite This: https://dx.doi.org/10.1021/acsami.0c09719



ACCESS

III Metrics & More

ABSTRACT: A detailed theoretical model and experimental study are presented that formulate and prove the existence of a robust ponderomotive force (PMF) near the interfaces in a granular dielectric material under microwave radiation. The model calculations show that the net direction of the PMF is pore angle-dependent. For most of the pore angles, the net force is towards the interface creating a mass transport that fills the interfacial pores and facilitates densification. For small ranges of angles, near 180° and 360°, PMF drives the ions in the reverse direction and depletes



Article Recommendations

the pores. However, the net force for such ranges of angles is small. The PMF also enhances the diffusion of the mobile ionic species and, consequently, accelerates the solid-state reaction by increasing the collision probability. The proof-of-concept experiments show that a mixture of elemental powders can diffuse, react, and form dense materials when radiated by the microwave in just a few minutes. Such characteristics, together with field-induced decrystallization, offer a novel and simple approach for the synthesis of nanostructured compounds, which can have practical implications in ceramic technologies and thermoelectric materials.

KEYWORDS: interfacial ponderomotive force, electromagnetic wave interaction with materials, microwave sintering, solid-state reaction, ceramics, thermoelectrics

1. INTRODUCTION

Microwave (MW) material processing has been considered from the 1950s and has emerged in producing different materials, such as ceramics, metals, semiconductors, and composites. MW energy is introduced as a non-ionizing form of electromagnetic radiation, working at a wavelength range of 1 m-1 mm and frequencies from 300 MHz to 300 GHz, respectively. MW electromagnetic radiation is caused by the combination of both oscillating electric and magnetic fields, propagating through an empty space. In a MW thermal synthesis process, the materials are heated up by volumetrically absorbing the electromagnetic energy to the sintering or alloying temperatures. The temperature rise is usually due to the interaction of MW with dipoles and charged particles, which results in dielectric or conductive losses and, eventually, heating of the materials.

In the practical applications, in comparison to the regular furnace in which the heat direction is from outside to inside, in a MW furnace, the heat flows from inside to outside. However, the nonthermal effects of the MW are often extraordinary and not wholly understood. There have been studies to attribute them to molecular agitation, localized heating, or thermally driven mass transport properties. ^{17–20}

According to the experimental reports, ^{21–26} many such effects follow nonequilibrium thermodynamics where the temperature cannot be well defined; hence, they require a different scope of understanding than the thermal effects. Phenomena, such as field-induced decrystallization, ^{27,28} field-induced reduction of graphene oxide, ²⁹ orders of magnitude enhancement in reaction rates, ^{30–33} unusually large or small MW absorption of some transition metal compounds, ³⁴ or dissolution of solid-solution alloys ^{35,36} invoke a new insight to understand the nonthermal MW effects.

Recent interest in self-powered wearables has seen thermoelectrics as a viable option to harvest body heat.³⁷ In pursuing and developing efficient thermoelectric (TE) compounds, researchers have studied several strategies in enhancing the thermoelectric performance via microstructure modification.^{37–41} In this regard, the MW sintering technique can

Received: May 27, 2020 Accepted: October 9, 2020



play a significant role in rapid sintering and providing the desired microstructure of the thermoelectric compounds. The application of field-induced decrystallization for the thermoelectric material synthesis is of particular interest since the grain size can have a significant impact on the efficiency of the material. 42-49 Furthermore, high density is often desired to obtain a high electrical conductivity. Densification generally requires a hot-pressing step, which can result in grain growth. 50 The rapid heating and field quenching enabled by MW radiation not only can reduce grain growth 17 but the decrystallization effects of the MW can also further create amorphous domains and reduce the grain size.²⁷ Finally, the field-induced accelerated diffusion can result in a fast solidstate reaction, which can be employed to form alloys from elements in less time and a more energy-efficient way.⁵¹ Another advantage is that the reaction happens below the melting point. Therefore, it eliminates the need for melt alloying and the subsequent ball milling, which is also a significant time and energy saving. There are several experimental demonstrations of the MW specific effects for thermoelectric material synthesis. For example, Birkel et al. 52 produced TiNiSn by a rapid MW reaction, with the high thermoelectric power factor of 2 mW/mK² at temperatures in the range of 700 to 800 K, and zT values of around 0.4, higher than conventionally prepared samples. The samples prepared using the MW method had a lower thermal conductivity compared to a conventionally prepared sample, which contributed to a higher zT value. In another experiment, Fan et al.⁵³ developed p-type Bi_{0.4}Sb_{1.6}Te₃ alloys by mechanical alloying followed by MW-activated hot pressing (MAHP). The results showed an enhancement in the phonon scattering and the reduction of the lattice thermal conductivity as low as 0.41 W/mK at 100 °C. This observation was related to the ultrafine microstructure maintained at a low sintering temperature.

Theoretical studies about the effect of high-frequency electromagnetic fields on a material, such as MW heating, have attracted much attention to understand the underlying physics. The understanding of the interactions between the oscillating fields and the ions in a material demands for a frequency-dependent model that can describe the experimental results. In general, the frequency of the electromagnetic field can affect the material in the following ways: (i) The dielectric absorption increases with frequency, (ii) the loss tangent increases with frequency; consequently, the MW penetration in conductive materials decreases due to the skin effect, 54,55 and (iii) the ponderomotive force (PMF) decreases with the frequency. Therefore, depending on the material size and properties, there is usually an optimum frequency that MW is absorbed, penetrates volumetrically inside the material, or applies an effective PMF. In this study, we will focus on the third effect, i.e., the characteristics of the PMF induced by the MW radiation. The first and second effects are well known and can be found in electromagnetic textbooks. 56,57

In plasma physics, the well-known PMF plays a vital role in ion migration and particle transport influenced by high-frequency, nonlinear electromagnetic fields. In solid-state materials, due to a highly packed structure, the ion migration, diffusion, and densification are not as smooth as in plasma, but the process rate and mass transport have been enhanced as a result of the PMF related to the electromagnetic fields in the MW heating process. S9,60 The quadratic dependence of the PMF to the charge yields the same direction of movement for

both positive and negative charges and, consequently, promotes their parallel migration and not their separation.

In this article, we provide a model to explain some of the field-induced observations based on the PMF, both theoretically and numerically. This model focuses on quantifying the PMF in granular materials and its pore angle dependency. We derive the strength and the direction of the PMF in a given material and explain its effect on ionic migration near the pores, leading to pore filling and densification. Moreover, the model shows enhanced ionic diffusion at interfaces, which can promote the solid-state reactions. A good follow-up work based on the theory presented here is studying the interdiffusion coefficients in solid solutions, where diffusion couples is an effective approach. 61,62 There is a large number of publications that have already studied the interdiffusions in solids under MW heating. 41,63,64 Whittaker's 65 study of the anisotropic diffusion in an experiment similar to the diffusion couples can be an excellent reference. The study focuses on the influence of MW radiation at the interparticle boundary and the directional dependency of the ionic migration on the external field. Whittaker's study concurs with a PMF-based model, similar to this work, to explain the nonthermal effect of the enhanced ion mobility at interfaces.

Finally, to confirm the PMF model, we have also investigated the MW sintering process of TE compounds. A range of different TE alloys with various physical properties were synthesized with MW and analyzed in detail to represent the generality of this method. It shows that a combination of densification accelerated diffusion and decrystallization effects of the MW lead to the formation of dense samples from elemental powders of various materials.

2. THEORY OF THE FIELD-INDUCED DENSIFICATION MECHANISM

2.1. Formalism. The densification and ion migration near the interfaces or physical surfaces of granular materials can be explained by the existence of a ponderomotive force. Booske et al. derived an approximate formula for the PMF by solving three essential equations, namely, drift-diffusion, continuity, and Poisson's equations:

$$\mathbf{J}_{i} = -D_{i} \nabla n_{i} + \frac{D_{i} n_{i}}{kT} q_{i} \mathbf{E} \tag{1}$$

$$\frac{\partial n_i}{\partial t} + \nabla J_i = 0 \tag{2}$$

$$\nabla E = \frac{1}{\epsilon} \sum_{i} q_{i} (n_{i} - n_{i}^{(0)})$$
(3)

where J, q, E, k, T, i, n, D, and ϵ are the flux of charged particles, the charge of elements, electric field, Boltzmann's constant, temperature, mobile charge species, concentration, diffusion coefficient, and the dielectric constant of the medium, respectively. After averaging eqs 1-3 over a period of the oscillation and expanding the J, n, and E to the second-order, where the static solutions, the high-frequency fluctuation, and the period-averaged are related to the zero, first, and second-order, respectively; eq 4 is derived for the quasi-stationary flux:

$$J_{i}^{(2)} \approx -D_{i} \nabla n_{i}^{(2)} + \frac{D_{i} n_{i}^{(2)}}{kT} q_{i} E^{(2)} + \frac{D_{i} n_{i}^{(0)}}{kT} \left\langle \left(\frac{n_{i}^{(1)}}{n_{i}^{(0)}} \right) q_{i} E^{(1)} \right\rangle$$
(4)

In this study, by assuming the homogeneity of the material, the first term is negligible, and the second term is also minor over the period on average. Thus, the dominant term of eq 4 is the last term, which contains the time average over the period of a high-frequency oscillating field in the angular brackets and explains a nonzero, significant ionic diffusion and mass transport near the boundaries in a granular material. After taking the time average of the last term and replacing the high-frequency charge density perturbation $n^{(1)}$ with $\frac{\epsilon}{2} \frac{\partial E^{(1)}}{\partial x}$, a force proportional to the gradient of E^2 is yielded:

PMF
$$\propto \left\langle \frac{\epsilon}{2} \frac{\partial |\mathbf{E}^{(1)}|^2}{\partial x} \right\rangle$$
 (5)

Such an approximate form of the PMF in solids is similar to the one in conventional plasma physics, where a non-uniform, high-frequency electromagnetic field derives the ionic transport and charged particle movement. Accordingly, in solids, the flux of charged particles, J, corresponds to the significant diffusion term, which is generated by a field-induced PMF, especially near the physical interfaces based on eqs 4 and 5. Since the PMF is proportional to the gradient of E^2 and the square of charge, its direction is the same for both positive and negative ions according to $f_p = -q^2 \nabla E^2/4m\omega_p^2$, where m is the mass of the particle, and ω_p is the plasma frequency.

To gain insight into the mechanisms behind the field-induced densification in solids, we evaluated the PMF exerted on the charged species, such as electrons, ions, or charged vacancies, by the MW radiation during sintering. We found that an intense MW field can create a strong force that promotes ionic transport. As we will show, the direction of the PMF in most cases is such that it moves the ions toward the interface, which results in filling the pores and densifying the material. The PMF has previously been derived from the Euler hydrodynamics model by Booske et al.:

$$f_{\mathbf{p}} = -\frac{\omega_{\mathbf{p}}^{2}}{\omega^{2} + \vartheta^{2}} \nabla \left\langle \frac{\epsilon \mathbf{E}^{2}}{2} \right\rangle + \frac{\omega_{\mathbf{p}}^{2}}{\omega^{2} + \vartheta^{2}} \vartheta \langle \epsilon \mathbf{E} \times \mathbf{B} \rangle \tag{6}$$

In deriving the approximate expression for the PMF, a study⁶⁶ assumes a single charge species (ions) and ignores the force due to the magnetic component of the MW radiation. Here, we start with both the electric and the magnetic fields and use a more general formalism based on the coupled equations of motion for electrons and ions to describe the PMF:

$$f = \frac{\omega_{\rm p}^2}{(\omega^2 + \vartheta^2)} \left[-\varepsilon_0 \frac{1}{2} \nabla \mathbf{E}^2 + (1 + \mu_{\rm r}) \varepsilon_0 \mu_0 \vartheta \mathbf{E} \times \mathbf{H} \right]$$
$$- i \frac{\omega_{\rm p}^2}{(\omega^2 + \vartheta^2)} \left[\frac{\vartheta \varepsilon_0}{2\omega} \nabla \mathbf{E}^2 + (1 + \mu_{\rm r}) \varepsilon_0 \mu_0 \omega \mathbf{E} \times \mathbf{H} \right]$$
(7)

To find the electric and magnetic fields, we assume a homogeneous material and solve the Maxwell equation in the quasi-static condition. Under these conditions, $\nabla \times E \approx 0$ and the magnetic field, which has constant intensity, can be ignored; therefore, the first term that relates to the gradient of the square of the electric field is dominant in both real and imaginary components. Consequently, in this case, both PMF eqs 6 and 7 have a similar dominant real term; however, in eqs 6, the imaginary term has been neglected. In this study, both

the real and imaginary parts of the dominant term ∇E^2 in eq 7 are taken into account. The imaginary term is generally smaller than the real part due to the coefficient $\frac{\vartheta}{\omega}$; however, as we will show, it influences the direction of the PMF near the interface. To find the magnitude and direction of the electric field, the Laplace's equation $\nabla^2 \Phi = 0$ is solved in the cylindrical coordinate of (r, φ, z) . The solution for the electric potential is

$$\Phi(r, \varphi) = \sum_{\alpha, \beta=0}^{\infty} \left[(Ar^{\alpha} \sin \alpha \varphi + Br^{\beta} \cos \beta \varphi) + (Cr^{-\alpha} \sin \alpha \varphi + Dr^{-\beta} \cos \beta \varphi) \right]$$
(8)

where r and φ are the radius of the pore and the azimuthal angle, respectively. A, B, C, and D are constant coefficients determined by the boundary conditions. α and β are the smallest positive roots that satisfy the boundary conditions. As illustrated in Figure 1, we assume a pore angle φ_0 surrounded

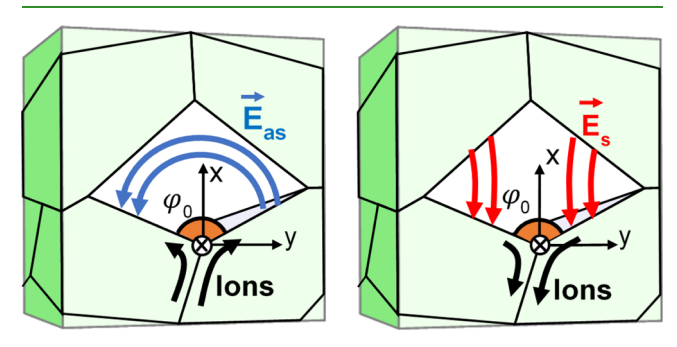


Figure 1. Direction of the asymmetric (E_{as}) and symmetric (E_s) modes of the electric field inside the pore between the grain boundaries and the corresponding ion movements when φ_0 <180°.

by a solid material volume. In the vicinity of the pore, $r \to 0$; therefore, C and D coefficients in eq 8 must be zero to prevent field divergence. The electric potential inside the grain can be written by some normalization as

$$\Phi(r,\,\varphi) = \acute{A}r^{\alpha} \frac{\sin\,\alpha(\pi - \varphi/2)}{\sin\,\alpha(\pi - \varphi_0/2)} + \acute{B}r^{\beta} \frac{\cos\,\beta(\pi - \varphi/2)}{\cos\,\beta(\pi - \varphi_0/2)}$$

where the first and second terms represent the asymmetric and symmetric modes of the electric potential inside the solid material. The asymmetric and symmetric modes of the electric field inside the pore, $|\varphi| \leq \frac{\varphi_0}{2}$, can be found per $E = -\nabla \Phi$. By converting from cylindrical to cartesian coordinates, we can show the field's direction at the particular symmetry plane of $\varphi = 0$ as

$$\mathbf{E} = -A\alpha r^{\alpha - 1}\hat{\mathbf{y}} - B\beta r^{\beta - 1}\hat{\mathbf{x}} \tag{10}$$

where the negative \hat{y} direction shows the asymmetric mode and negative \hat{x} direction represents the symmetric one, as shown in Figure 1.

We solve for the electric field for half of the pore and the material, and the other half, depending on the pore symmetry, can be similar or different. Therefore, inside the material volume, i.e., $\frac{\varphi_0}{2} < \varphi \leq \pi$, we have

$$\begin{split} E &= - \hat{A} \alpha r^{\alpha - 1} \frac{\sin \alpha (\pi - \varphi/2)}{\sin \alpha (\pi - \varphi_0/2)} \hat{r} \\ &+ \hat{A} \alpha r^{\alpha - 1} \frac{\cos \alpha (\pi - \varphi/2)}{\sin \alpha (\pi - \varphi_0/2)} \hat{\varphi} \\ &- \hat{B} \beta r^{\beta - 1} \frac{\cos \beta (\pi - \varphi/2)}{\cos \beta (\pi - \varphi_0/2)} \hat{r} \\ &- \hat{B} \beta r^{\beta - 1} \frac{\sin \beta (\pi - \varphi/2)}{\cos \beta (\pi - \varphi_0/2)} \hat{\varphi} \end{split} \tag{11}$$

Per the boundary conditions for the tangential and normal components, $\hat{A} = A$, $\hat{B} = B$, and α and β must satisfy the following two equations:

$$\operatorname{Etan} \alpha(\varphi_0/2) = -\tan \alpha(\pi - \varphi_0/2) \tag{12}$$

$$\tan \beta(\varphi_0/2) = -\epsilon \tan \beta(\pi - \varphi_0/2) \tag{13}$$

Therefore, the asymmetric mode, which is in the negative y direction, diverges to infinity when $r\rightarrow 0$. The symmetric mode, however, approaches zero when $r\rightarrow 0$.

2.2. Case Study: Quantification of the PMF in Bi_{0.5}Sb_{1.5}Te₃ Thermoelectric Alloy. As discussed, in a uniform medium, a uniform flux of charged particles can be generated by a high-frequency harmonic electric field. Near the interfaces or the grain boundaries, due to the medium discontinuity, the field flux is non-uniform. This non-uniform field generates a PMF that can result in the transport of ionic concentration away or toward the interface, hence, depleting or filling the pores, respectively. To quantify the effect of the mass transport and ion migration under the MW radiation, we calculate the electric field and the corresponding PMF in MWprocessed Bi_{0.5}Sb_{1.5}Te₃ thermoelectric alloy. The boundary conditions, material properties, MW intensity, and polarization were taken into account in the calculations. Different components of the PMFs were calculated inside the grain at $r = 1 \mu m$ away from the interface. The calculations were done at T = 450 °C. We further investigate the effect of the pore angles on the PMF.

The electric field intensity was considered to be 10^5 V/m based on the MW power in the setup discussed in the experimental section. The collision frequency was assumed to be approximately 1/10 of the plasma frequency. The energy gap, dielectric constant, molecular mass, and the magnetic permeability of the alloy are the other parameters used in this calculation, as listed in Table 1.

Figure 2a shows the magnitude of the electric field for the symmetric and asymmetric modes versus the distance from the pore (r) for some given pore angles such as 80° , 180° , and 280° . As it is inferred from Figure 2a, for small pore angles, the

Table 1. Process and Material Parameters of the $Bi_{0.5}Sb_{1.5}Te_3$ Sample

parameters	value	parameters	value
field intensity (V/m)	10 ⁵	molar mass (kg/mol)	0.1340
process temperature (°C)	450	MW frequency (Rad/s)	1.5×10^{10}
energy gap (eV)	0.24	plasma frequency (Rad s ⁻¹)	3.5×10^{10}
dielectric constant	96.9	collision frequency (Rad s^{-1})	3.5×10^9
mass density (g/cm ³)	3.4		

magnitude of the asymmetric electric field mode, $E_{\rm as}$ (solid blue line), is about two-three orders of magnitude larger than the symmetric mode, $E_{\rm s}$ (dashed blue line). For the straight pore angle ($\varphi_0=180^\circ$), both $E_{\rm as}$ (solid red line) and $E_{\rm s}$ (dashed red line) are constant over r, but in this case the symmetric mode is larger. For a reflex angle like 280° , $E_{\rm s}$ (dashed purple line) stays larger than the $E_{\rm as}$ (solid purple line) by about an order of magnitude with inverse slopes.

Figure 2b illustrates the trends of the $E_{\rm as}$ and $E_{\rm s}$ versus the pore angle φ_0 . It can be seen that there is a cross-point (φ_0 = 168°) at which the magnitude of $E_{\rm as}$ and $E_{\rm s}$ switches; therefore, for the pore angles less than 168° , the asymmetric mode is dominant with a maximum value at around φ_0 = 20° , but after the cross-point up to φ_0 = 358° , the symmetric mode is more effective with a turning point at 180° , where $E_{\rm s}$ diverges. For φ_0 = 358° – 360° the asymmetric mode becomes dominant again.

Figure 3a depicts the amplitude of the PMF corresponding to the symmetric and asymmetric modes of the electric field. The angular components of the PMF are zero due to the gradient of E^2 not being a function of the angle in this case. It is seen that the PMF has its highest value at the corner of the pore and then decreases with a smooth slope when moving away from the corner. By comparing the forces along the pore angle, it is evident that there are four regions, from zero to a cross-point at about $\varphi_0 \approx 168^{\circ}$, the cross-point to the straight angle, the reflex angles up to $\varphi_0 = 358^{\circ}$, and angles with $\varphi_0 =$ $358^{\circ} - 360^{\circ}$, respectively. In the first region, low angles, F_{as} is larger than F_s due to the larger gradient of E_{as}^2 . At the crosspoint $\varphi_0 \approx 168^\circ$, \mathbf{F}_{as} and \mathbf{F}_{s} become equal; it is notable that the position of the cross-point angle is a function of the amplitudes of the electric fields, A and B, with a small relative sensitivity around 0.045; however, its value is independent of the material properties, such as the dielectric constant, collision frequency, or the density. In the region from $\varphi_0 \approx 168^{\circ}$ to 180° , the symmetric mode will be dominant. Both F_s and F_{as} have a turning point at $\varphi_0 = 180^{\circ}$, where both E_s and E_{as} are constant over r. Then for the reflex angles $>180^{\circ}$, the symmetric mode remains dominant up to $\varphi_0 = 358^{\circ}$, and finally in the fourth region, $\varphi_0 = 358^{\circ} - 360^{\circ}$, the asymmetric mode prevails again.

Figure 3b shows the angles of the forces \mathbf{F}_s and \mathbf{F}_{as} versus the pore angle φ_0 . According to eq 7, the ratio of the imaginary and real parts of the PMF is a constant coefficient, ϑ/ω , which results in a constant angle for the forces. Thus, for $\varphi_0 < 180^\circ$, the \mathbf{F}_{as} direction is θ_0 , while the angle of \mathbf{F}_s is $\pi - \theta_0$, and for $\varphi_0 > 180^\circ$, these directions are inversed. For better visualization, the directions of the PMFs are shown in the insets of Figure 3b

Figure 3c illustrates the direction of the PMF for some given different pore angles, and consequently, the direction of the ion transport near the interfaces of the grain boundaries for both asymmetric and symmetric modes (the blue and red arrows, respectively). For the asymmetric mode, at φ_0 <168°, PMF has θ_0 deviation from $\varphi_0 = 0^\circ$; therefore, the PMF tends to fill the pore by extracting materials from the inter-grain boundary, easing the pore shrinkage. Then, for the pores with $\varphi_0 \approx 168^{\circ} - 180^{\circ}$, although F_{as} is in the same θ_0 direction and fills the pore, it is not the dominant mode up to $\varphi_0 = 358^{\circ}$. At reflex angles of $\varphi_0 = 180^{\circ} - 358^{\circ}$, the asymmetric force changes its direction to $\pi - \theta_0$ and drives the ions away from the interface toward the bulk of the material. Hence, \mathbf{F}_{as} tends to deplete the pores, but its magnitude is smaller than F_s . At φ_0 = $358^{\circ} - 360^{\circ}$, F_{as} becomes dominant again with a direction along $\pi - \theta_0$, which still inclines to deplete the pore.

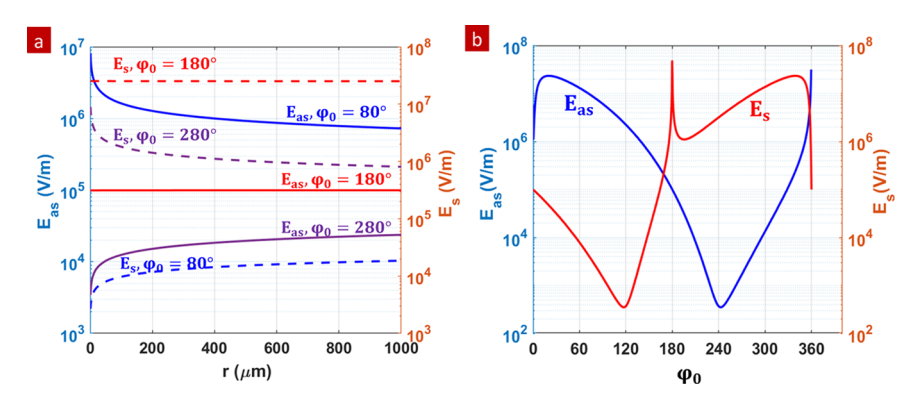


Figure 2. Electric field amplitudes for symmetric (E_s) and asymmetric (E_{as}) modes versus (a) the distance from the pore corner and (b) the pore angle.

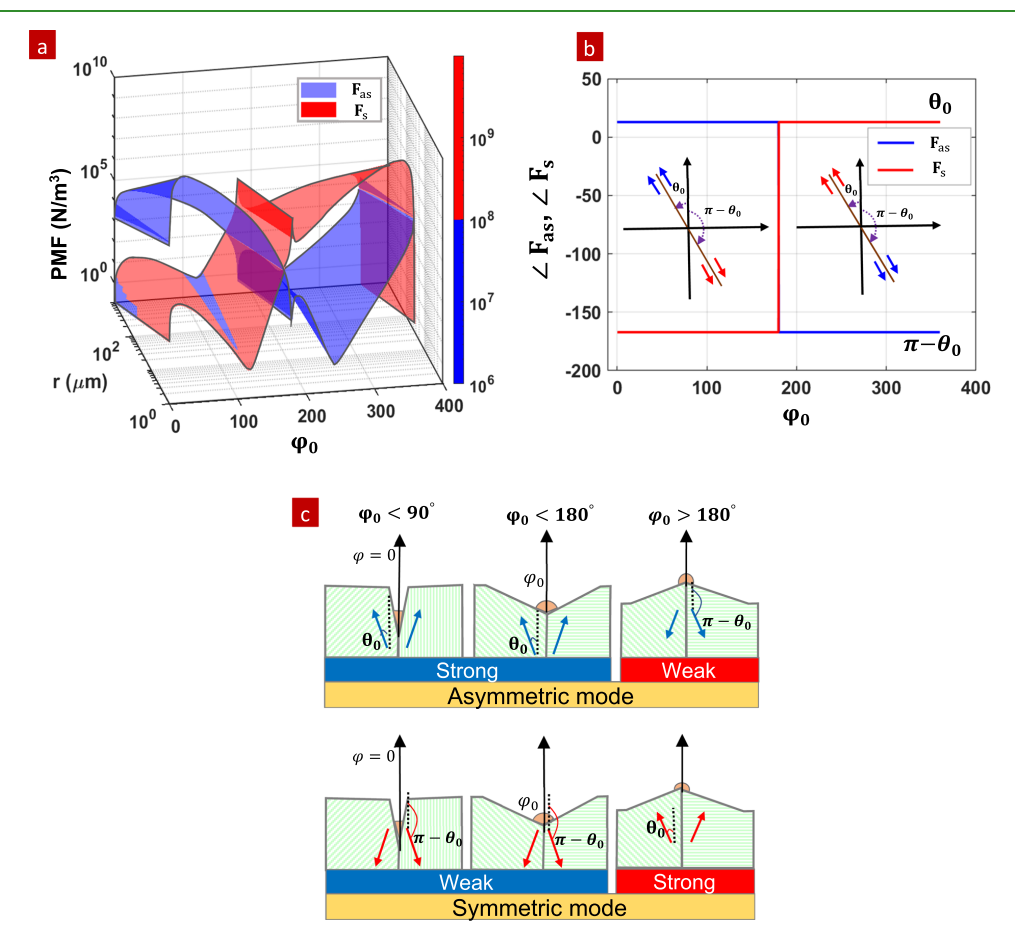


Figure 3. Asymmetric and symmetric modes of (a) the amplitude of the PMF per unit volume, (b) the PMF direction versus the pore angle, the insets show these directions in polar coordinates, and (c) the PMF and the corresponding direction of the ionic transport for several pore angles at the grain boundaries.

For the symmetric mode, the process is reversed, i.e., the PMF is at the $\pi-\theta_0$ angle and tends to deplete the pore when $\varphi_0{<}168^\circ$, although not being the dominant mode. At $\varphi_0\approx 168^\circ-180^\circ$, \mathbf{F}_s is still in the same direction and depletes the pore while it is also dominant. Above these angles, within $\varphi_0=180^\circ-358^\circ$, \mathbf{F}_s stays dominant but changes its direction to θ_0 and fills the pore. At last, for pore angles of $\varphi_0=358^\circ-360^\circ$, the symmetric mode becomes smaller than \mathbf{F}_{as} while staying in the same direction. It is worth noting that θ_0 is a material and a MW frequency-dependent angle that is determined by the ϑ/ω ratio.

It is worth summarizing the net PMF for different pore angles. For small angles of less than 168°, the asymmetric mode force is dominant ($F_{as}\gg F_s$), and the net PMF fills the pores and densifies the material. For reflex pore angles, the directions of both F_s and F_{as} reverses, and in the range of φ_0 = $180^\circ-358^\circ$, F_s is dominant ($F_s\gg F_{as}$), and the net PMF again pulls out the ions from the bulk of the material toward the interfaces and fills the pores. Only for two small ranges of the pore angles, from the first cross-point to the straight angles, here $\varphi_0\approx 168^\circ-180^\circ$, and from the second cross-point to 360° , here $\varphi_0=358^\circ-360^\circ$, the dominant force, F_s and F_{as} , respectively, tend to deplete the pore. It should be noted that

near the cross points, the net PMF is small; as such, the pore depletion is a weak process.

Overall, the net PMF tends to fill the pores for most pore angles. Only for a small range of pore angles, the net PMF tends to deplete the pores, however, in a much weaker strength. The process is the same for both positive and negative charges as the PMF depends on $q^2\nabla E^2$.

It should be noted that this study is for a specific configuration of the general case. For a general solution, the electric field, which is derived from eq 8, is a sum of many terms with different coefficients, which must be determined according to the boundary conditions for the given system. Therefore, the angles in Figure 3, where the pore filling and depleting processes change trends, apply only to the particular assumed configuration; otherwise, they can change for various systems depending on the grain shape, size, MW field direction, polarization, etc.

In solid-state reactions, due to the dense packing structure, compared to the gas, liquid, or plasma phase, reaction process rates, such as mixing and collision, and the probability of a reaction per near-encounter are transport limited, as schematically shown in Figure 4. As discussed, the dominant term of eq

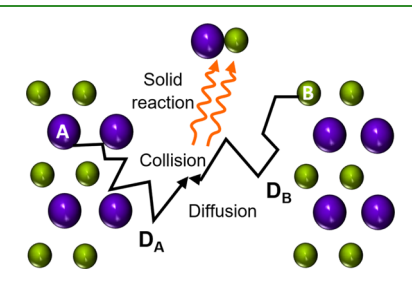


Figure 4. Mixing, collision, diffusion, and solid-state reactions of solid reactants A and B.

4 expresses the correlation between the flux of charged particles, *J*, and the nonzero ionic diffusion and mass transport. As noted, the diffusion of the mobile species can be significantly enhanced by the driving force due to the MWs, i.e., the field-induced PMF accelerates diffusion and consequently speeds up the solid-state reaction. It is evident that the PMF can simultaneously densify the granular materials, increase ionic diffusion, and enhance the solid-state reaction rates by enhancing the collision rates.

In the following, we present several experiments that demonstrate the effect of MW radiation on the solid-state reaction and densification. These experiments provide the first evidence that solid-state reactions and densification can be enhanced simultaneously by MWs.

3. MATERIALS AND METHODS

For the proof of concept, MW synthesis of four different materials was investigated. Elemental powders of Bi (99.99% purity), Sb (99.99% purity), Te (99.99% purity), Mn (99.99% purity), and Cr (99.99% purity) were mixed in a desired stoichiometric ratio using a vibratory mixer (Spex milling/mixing machine) to prepare the mixed powder of Bi_{0.5}Sb_{1.5}Te₃, Sb₂Te₃, CrSb, and MnTe. They were loaded in steel jars with steel balls of 10 mm in diameter with a ball to a powder ratio of approximately 1:1 inside a glove box with an argon environment. The mill was operated for 15 min to ensure uniform mixing without alloying. The mixed powders were loaded into a stainless steel die, with an inner diameter of 6 mm, and cold-pressed to form cylindrical samples with a density of ~70 to 80%. The cold-pressed samples were then loaded into a boron nitride die, which was further loaded into

quartz tubes. The tube was evacuated and purged three times with nitrogen gas and finally filled to a pressure of 600 Torr. These quartz tubes were loaded into a rectangular MW single-mode cavity attached to a 2.45GHz (1 kW) magnetron powered by a variable voltage source (Figure 5). The material was processed in a mixed field. Details

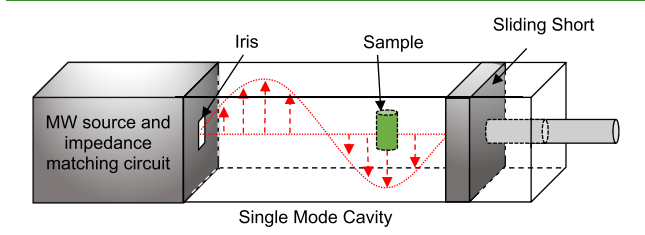


Figure 5. Schematic of the single-mode MW cavity used in all experiments.

about the reactor can be found in the Ph.D. theses by Nozariasbmarz and Malhorta. 67,68 The powders and samples were characterized by Xray diffraction (XRD) (Rigaku benchtop). Discs of 800 μm thickness were cut and polished from the samples for thermal diffusivity measurements using a Linseis LFA-1000 system. The crystal microstructure was studied with the FEI Talos F200X transmission electron microscope (TEM).

Figure 6 represents the typical heating profile of a sample (Sb₂Te₃) under MW radiation. The heating rate was maintained between 20-

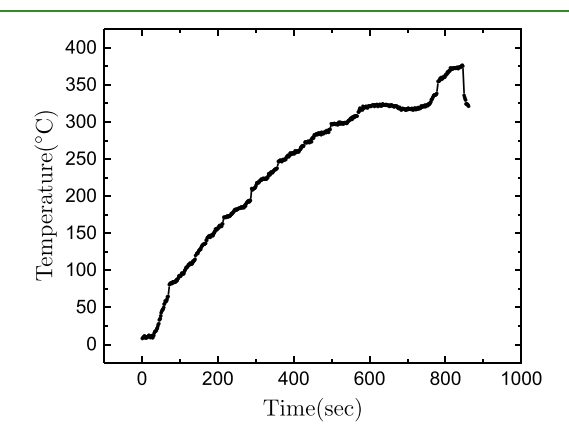


Figure 6. MW heating profile of a typical sample up to 375 °C.

30 °C/min, and the MW radiation was modulated with a duty cycle of 70% to ensure isothermal heating and avoid the formation of hotspots, which could give a false temperature reading since the pyrometer measures an average temperature across the sample. The power was shut down when the target temperature was reached. The sample cooled down rapidly by turning off the MW.¹⁷ This is especially advantageous in thermoelectrics since it can result in reduced grain growth.

4. RESULTS AND DISCUSSION

4.1. MW Synthesis of the Bi_{0.5}Sb_{1.5}Te₃ Thermoelectric Compound. Figure 7 illustrates the XRD data of four different Bi-Sb-Te samples, mixed elemental powders, and MW sintered at 350, 400, and 425 °C. The XRD analysis indicates the presence of Bi (012), Sb (012), and Te (011) elements in the as-mixed powder without any alloy phases. For the sample sintered at 350 °C, all the major peaks of the elements disappeared, and peaks for Bi_{0.5}Sb_{1.5}Te₃ are revealed, implying that the majority of the alloy has already formed. The time to reach the target temperature was less than 15 min, indicating a significantly enhanced solid-state reaction under the MW field. Since reaction rates are limited by the proximity

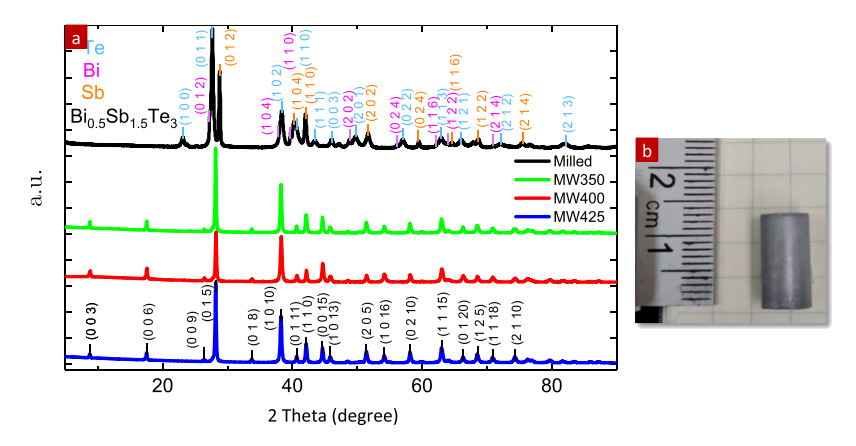


Figure 7. (a) XRD data of the initially mixed powder and the samples consolidated using MW sintering at 350, 400, and 425 °C; (b) MW-sintered bulk sample with 99% density.

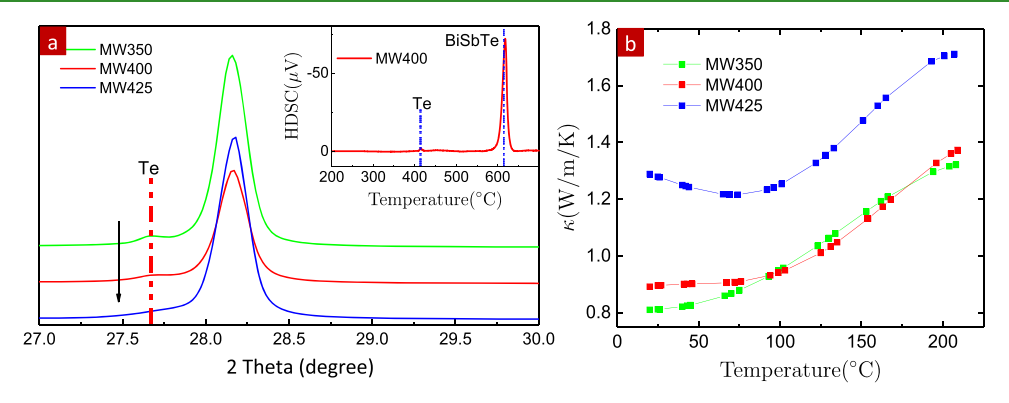


Figure 8. (a) XRD patterns for three different MW temperatures, and (b) thermal conductivities of sintered Bi_{0.5}Sb_{1.5}Te₃ samples.

of the charged species, the rapid solid-state reaction can be attributed to the enhanced diffusion that resulted from the interfacial PMF, as discussed in the previous section. The XRD analysis of the sample sintered at 425 $^{\circ}\text{C}$ shows a single phase of $\text{Bi}_{0.5}\text{Sb}_{1.5}\text{Te}_3$ with no secondary phase. This composition is in agreement with the original stoichiometry of the mixed powder.

A closer look at the main XRD peak of the Bi-Sb-Te alloy (Figure 8a) indicated some residual tellurium after the MW processing at 350 °C. The peak for this phase reduces in intensity for the sample MW sintered at 400 °C. The differential thermal analysis of sample MW at 400 °C, shown in Figure 8(a), also indicates a sharp peak corresponding to the Bi-Sb-Te alloy. A small peak for tellurium is also observed, in agreement with the Te line seen in the XRD data. The Te line completely disappeared when the sample was sintered using MW at 425 °C. During the heating of the sample under the MW, it was observed that all the samples start shrinking at around a temperature of 325 °C. Interestingly, there was no noticeable mass change; hence, the shrinking was due to densification. It is worth noting that the force applied to the sample during the processing was approximately 50-60 kPa axially using a spring. Compared to traditional sintering pressures of several 10 MPa, this pressure is negligible and cannot explain the observed significant densification. As discussed earlier, the PMF near the grain boundaries enhances ion migration toward the pores, which can fill the pores and cause the volumetric shrinkage of the sample. The mass density improved from ~80 up to 99% for the sample sintered at 425 °C. The density obtained under the MW is in the range of or

better than the values obtained by spark plasma sintering of a similar powder.

The decrystallization was also observed for this material resulting in a small thermal conductivity, as shown in Figure 8b. The larger thermal conductivity of the sample MW at 425 $^{\circ}$ C may be due to the partial grain growth at higher temperatures and a larger electronic thermal conductivity. The crystallinity analysis of the XRD data, using the Halder–Wagner model, supports this observation. Based on the model, the sample has average grain sizes of 32 and 36 nm for temperatures of 400 and 425 $^{\circ}$ C, respectively. A TEM study of the sample MW at 400 $^{\circ}$ C (Figure 9) indicates a unit cell with a c dimension of 3 nm, which agrees with the literature for this material. Figure 10 shows SEM images of the fractured surface of an MW sample processed at 400 $^{\circ}$ C. The

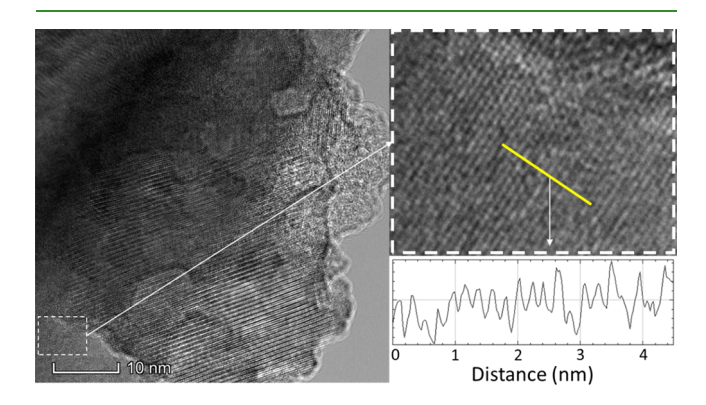


Figure 9. TEM image of the $Bi_{0.5}Sb_{1.5}Te_3$ sample sintered at 400 °C.

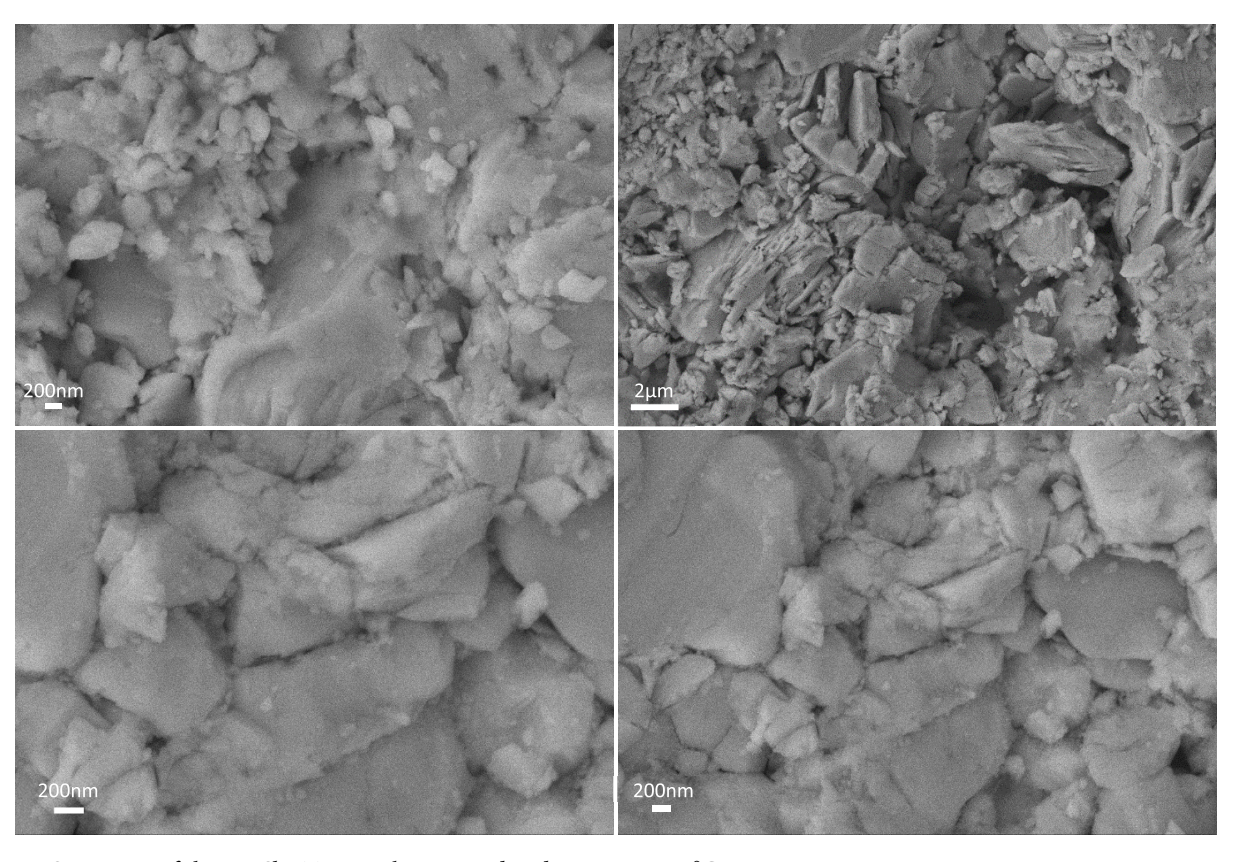


Figure 10. SEM scans of the Bi_{0.5}Sb_{1.5}Te₃ sample processed under MW at 400 °C.

micrograph shows sub-micrometer to several micrometer-sized grains. $Bi_{0.5}Sb_{1.5}Te_3$ is a soft anisotropic material with van der Waals bonds in the normal to the basal plane. As such, the fractured surface usually has a granular structure. The images confirm the sintering and high density of the samples prepared by MW processing, in agreement with the density measurements discussed earlier.

4.2. MW Synthesis of Several Other Compounds. Based on the successful rapid synthesis of $Bi_{0.5}Sb_{1.5}Te_3$ by MW, the technique was tested for the synthesis of three other compounds, including Sb_2Te_3 , CrSb, and MnTe. Like the synthesis of $Bi_{0.5}Sb_{1.5}Te_3$, the high purity elemental powders of these compounds were mixed according to the desired stoichiometry. Except for the process temperature (as shown in Table 2), all other steps are the same as the ones mentioned in the previous section for $Bi_{0.5}Sb_{1.5}Te_3$.

Table 2. Optimum MW Sintering Temperature of the Studied TE Compounds

TE compounds	$Bi_{0.5}Sb_{1.5}Te_3\\$	Sb_2Te_3	CrSb	MnTe
optimum $T_{\rm MW}$ (°C)	400	425	950	750

4.2.1. Antimony Telluride, Sb_2Te_3 . The XRD data of Figure 11 confirms the formation of a single-phase Sb_2Te_3 alloy at 400 and 425 °C. For the sample MW at 375 °C, a peak for the Sb_2Te_3 phase is present along with peaks for elemental Te and Sb. This indicates that the solid-state reaction has started to take place at lower temperatures. At 400 and 425 °C, however, there is no elemental peak regarding the Te or Sb elements.

4.2.2. Chromium Antimonide, CrSb. As shown in Figure 12, the solid-state reaction of CrSb started at 650 °C evidenced

by the appearance of the (101) diffraction line in addition to the lines for Sb and $CrSb_2$ phases. This reaction completes at 950 °C with the disappearance of the lines for the impurity phases. Figure 13 shows the evolution of peak intensities of the (012) diffraction line for Sb and (101) line for CrSb. It can be seen that upon increasing the temperature, the intensity of the Sb peak decreases, while that of CrSb increases with a rapid trend above 800 °C.

4.2.3. Manganese Telluride, MnTe. As the last example, MnTe was sintered with a similar approach using MW radiation. Figure 14 illustrates the XRD spectra of the MnTe compound at different sintering temperatures. It can be seen that the alloying is completed at a temperature of 750 °C. It is worth comparing this with the alloy formation using annealing in a conventional furnace. In a traditional method, the mixed powder of Mn and Te is annealed at about 750 °C for several days to form the complete alloy. Here, the alloy is formed under MW radiation at a similar temperature in only ~15 min.

To summarize, Table 3 compares the processing time and temperature of the tested compounds synthesized via MW and conventional methods. Compared with the processing methods using conductive heating, MW processing offers an extremely short processing time and low energy consumption. MW processing is a relatively new area with the promise of broad applications in chemical reactions and synthesis.

5. CONCLUSION

A theoretical model based on the interfacial ponderomotive force (PMF) was presented to explain the simultaneous densification and solid-state reaction under MW radiation. This model predicts pore shrinking due to MW field-induced ion migration near the interfaces. The model also predicts that

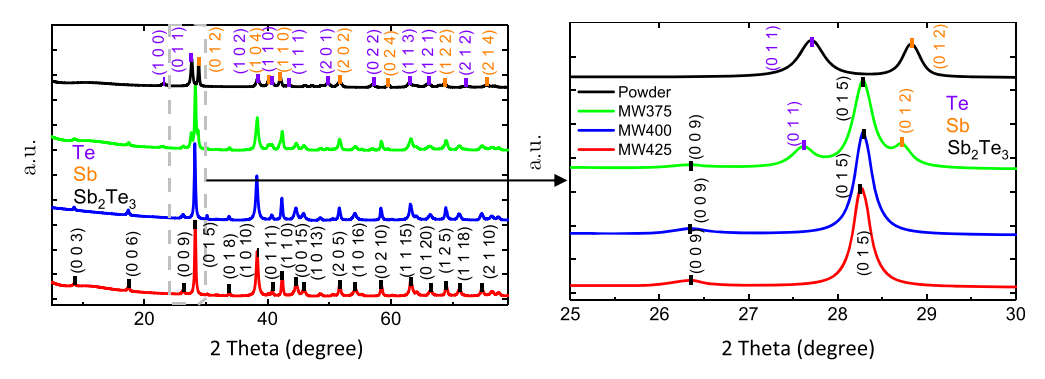


Figure 11. XRD data of Sb₂Te₃ elemental powder compared to powder MW sintered at three different temperatures: 375, 400, and 425 °C. The figure on the right highlights the changes in the composition with increasing sintering temperatures.

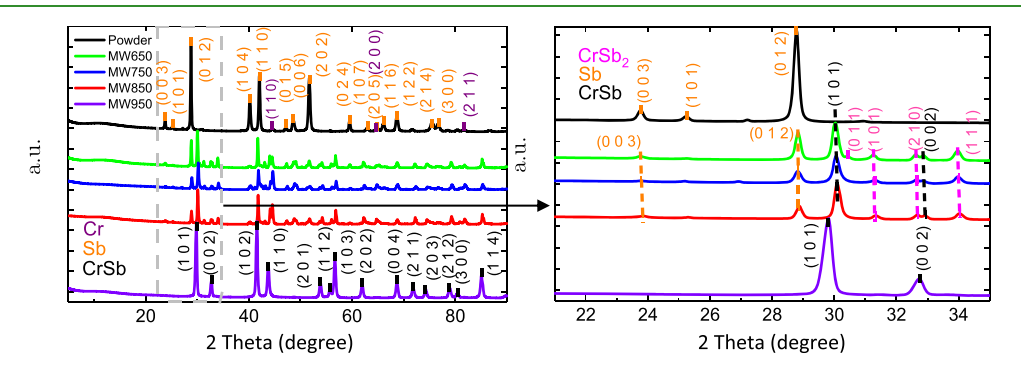


Figure 12. XRD analysis of the Cr-Sb study with a comparison of mixed powder with samples sintered at 650, 750, 850, and 950 °C.

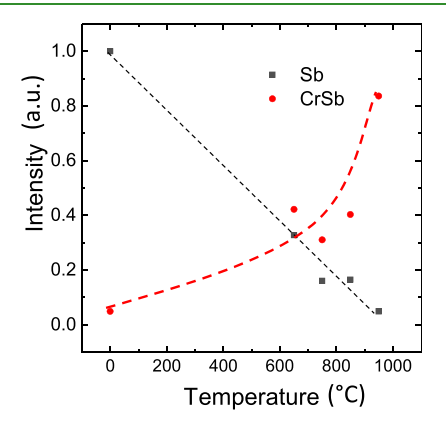


Figure 13. Comparison of relative peak intensities of Sb (012) and CrSb (101) vs the MW sintering temperature.

MW radiation can result in the enhancement of ion diffusion, which can increase the collision probability, hence the reaction

Table 3. Comparison of Time and Temperature for MW and Conventional Processing

	MW		conventional	
material	temperature (°C)	time (min)	temperature (°C)	time (hours)
$Bi_{0.5}Sb_{1.5}Te_3$	425	20	750	12-24
Sb_2Te_3	425	20	750	12-24
MnTe	750	30	950	48-72
CrSb	950	30	950	48-72

rates. To validate the model experimentally, we synthesized several binary and ternary compounds using MW sintering. In all cases, the solid-state reaction happened entirely in just a few minutes. Compared to conventional annealing methods, which can take several days to complete the reaction, this method offers significant time and energy saving. MW radiation also results in simultaneous densification and decrystallization,

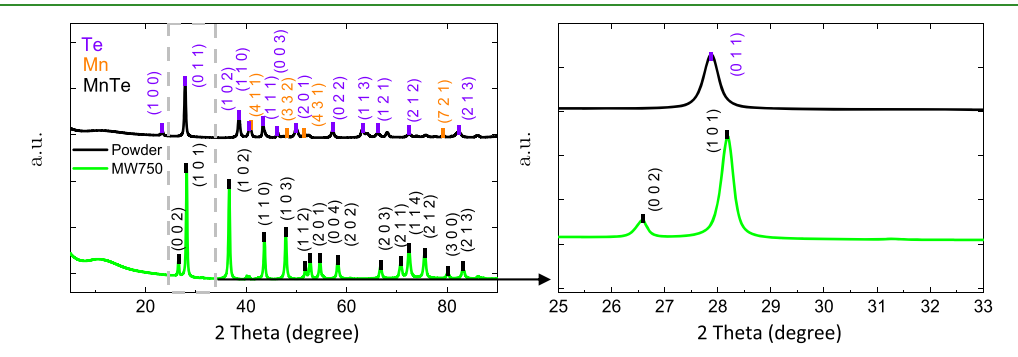


Figure 14. XRD analysis of the mixed Mn and Te powder and the MnTe compound formed at 750 °C under MW radiation.

which simplifies the synthesis of dense nanograined bulk samples for applications in ceramics and thermoelectrics.

AUTHOR INFORMATION

Corresponding Author

Daryoosh Vashaee — Department of Electrical and Computer Engineering and Department of Materials Science and Engineering, North Carolina State University, Raleigh, North Carolina 27606, United States; orcid.org/0000-0003-3667-3672; Phone: (919) 515-9599; Email: dvashae@ncsu.edu

Authors

- Abhishek Malhotra Department of Electrical and Computer Engineering, North Carolina State University, Raleigh, North Carolina 27606, United States
- Mahshid Hosseini Department of Materials Science and Engineering and Physics Department, North Carolina State University, Raleigh, North Carolina 27606, United States
- Sadeq Hooshmand Zaferani Department of Electrical and Computer Engineering, North Carolina State University, Raleigh, North Carolina 27606, United States; School of Mechanical Engineering, University of Adelaide, Adelaide, South Australia 5005, Australia
- Michael Hall Department of Materials Science and Engineering, North Carolina State University, Raleigh, North Carolina 27606, United States

Complete contact information is available at: https://pubs.acs.org/10.1021/acsami.0c09719

Author Contributions

¹A.M. AND M.H. contributed equally to this work.

Notes

The authors declare no competing financial interest.

■ ACKNOWLEDGMENTS

This study is partially based upon the work supported by the Air Force Office of Scientific Research (AFOSR) under the contract number FA9550-19-1-0363 and the National Science Foundation (NSF) under grant numbers ECCS-1351533, ECCS-1515005, and ECCS-1711253. This work made use of the instrumentation at AIF acquired and supported by NSF grants DMR-1726294 and ECCS-1542015.

REFERENCES

- (1) Clark, D. E.; Sutton, W. H. Microwave Processing Of Materials. *Annu. Rev. Mater. Sci.* **1996**, 26, 299–331.
- (2) Schiffman, R. F. Commercializing Microwave Systems: Paths To Success Or Failure. *Ceram. Trans.* **1995**, *59*, 7–17.
- (3) Katz, J. D. Microwave Sintering Of Ceramics. *Annu. Rev. Mater. Sci.* **1992**, 22, 153–170.
- (4) Mary, J. A.; Manikandan, A.; Kennedy, L. J.; Bououdina, M.; Sundaram, R.; Vijaya, J. J. Structure And Magnetic Properties Of Cu-Ni Alloy Nanoparticles Prepared By Rapid Microwave Combustion Method. *Transactions of Nonferrous Metals Society of China* **2014**, 24, 1467–1473.
- (5) Bao, R.; Yi, J. Densification And Alloying Of Microwave Sintering WC–8 Wt.%Co Composites. *Int. J. Refract. Hard Met.* **2014**, 43, 269–275.
- (6) Demirskyi, D.; Agrawal, D.; Ragulya, A. Neck growth kinetics during microwave sintering of nickel powder. *J. Alloys Compd.* **2011**, 509, 1790–1795.

- (7) Demirskyi, D.; Agrawal, D.; Ragulya, A. Neck formation between copper spherical particles under single-mode and multimode microwave sintering. *Mater. Sci. Eng., A* **2010**, 527, 2142–2145.
- (8) Agrawal, D., Microwave sintering of metal powders. In *Advances in powder metallurgy*; Woodhead Publishing 2013, pp. 361–379.
- (9) Prado-Gonjal, J.; Schmidt, R.; Morán, E. Microwave-Assisted Routes for the Synthesis of Complex Functional Oxides. *Inorganics* **2015**, *3*, 101–117.
- (10) Haque, K. E. Microwave energy for mineral treatment processes-a brief review. *Int. J. Miner. Process.* **1999**, *57*, 1–24.
- (11) Curnutte, B. Principles of microwave radiation. J. Food Prot. 1980, 43, 618-624.
- (12) Gupta, M.; Wong, W. L. E. Enhancing Overall Mechanical Performance Of Metallic Materials Using Two-Directional Microwave Assisted Rapid Sintering. Scr. Mater. 2005, 52, 479–483.
- (13) Das, S.; Mukhopadhyay, A. K.; Datta, S.; Basu, D. Prospects Of Microwave Processing: An Overview. *Bull. Mater. Sci.* **2009**, *32*, 1–13.
- (14) Agrawal, D. Microwave Sintering Of Ceramics, Composites, Metallic Materials And Melting Of Glasses. *Trans. Indian Ceram. Soc.* **2006**, *65*, 129.
- (15) Sutton, W. H. Microwave Processing Of Ceramic Materials. *Am. Ceram. Soc. Bull.* **1989**, *68*, 376–386.
- (16) Meng, J.; Pan, Y.-B.; Luo, Q.; An, X.-H.; Liu, Y.; Li, Q.; Chou, K.-C. A Comparative Study On Effect Of Microwave Sintering And Conventional Sintering On Properties Of Nd–Mg–Ni–Fe3O4 Hydrogen Storage Alloy. *Int. J. Hydrogen Energy* **2010**, 35, 8310–8316.
- (17) Kitchen, H. J.; Vallance, S. R.; Kennedy, J. L.; Tapia-Ruiz, N.; Carassiti, L.; Harrison, A.; Whittaker, A. G.; Drysdale, T. D.; Kingman, S. W.; Gregory, D. H. Modern Microwave Methods In Solid-State Inorganic Materials Chemistry: From Fundamentals To Manufacturing. *Chem. Rev.* **2014**, *114*, 1170.
- (18) Ma, J. Master Equation Analysis of Thermal and Nonthermal Microwave Effects. *Phys. Chem. A* **2016**, *120*, 7989–7997.
- (19) Jacob, J.; Chia, L. H. L.; Boey, F. Y. C. Review Thermal And Non-Thermal Interaction Of Microwave Radiation With Materials. *J. Mater. Sci.* **1995**, *30*, 5321–5327.
- (20) Mishra, R. R.; Sharma, A. K. Microwave—Material Interaction Phenomena: Heating Mechanisms, Challenges And Opportunities In Material Processing. *Composites Part A* **2016**, *81*, 78–97.
- (21) Nakamura, N.; Terban, M. W.; Billinge, S. J. L.; Reeja-Jayan, B. Unlocking the structure of mixed amorphous-crystalline ceramic oxide films synthesized under low temperature electromagnetic excitation. *J. Mater. Chem. A* **2017**, *5*, 18434–18441.
- (22) Kappe, C. O.; Pieber, B.; Dallinger, D. Microwave Effects In Organic Synthesis: Myth Or Reality? *Angew. Chem., Int. Ed.* **2013**, *52*, 1088
- (23) Ahirwar, R.; Tanwar, S.; Bora, U.; Nahar, P. Microwave Non-Thermal Effect Reduces ELISA Timing To Less Than 5 Minutes. *RSC Adv.* **2016**, *6*, 20850–20857.
- (24) Ayyappadas, C.; Raja Annamalai, A.; Agrawal, D. K.; Muthuchamy, A. Conventional And Microwave Assisted Sintering Of Copper-Silicon Carbide Metal Matrix Composites: A Comparison. *Metall. Res. Technol.* **2017**, *114*, 506.
- (25) Reeja-Jayan, B.; Harrison, K. L.; Yang, K.; Wang, C.-L.; Yilmaz, A. E.; Manthiram, A. Microwave-Assisted Low-Temperature Growth Of Thin Films In Solution. *Sci. Rep.* **2012**, *2*, 1003.
- (26) Manthiram, A., Jayan, B. R., Harrison, K. L. Growing Crystalline Semiconductor Oxide Thin Films On A Substrate At A Low Temperature Using Microwave Radiation US Patent App. 14/651,725 (2013).
- (27) Nozariasbmarz, A.; Dsouza, K.; Vashaee, D. Field Induced Decrystallization of Silicon: Evidence of a Microwave Non-thermal Effect. *Appl. Phys. Lett.* **2018**, *112*, 093103.
- (28) Roy, R.; Peelamedu, R.; Hurtt, L.; Cheng, J.; Agrawal, D. Definitive experimental evidence for Microwave Effects: Radically new effects of separated E and H fields, such as decrystallization of oxides in seconds. *Mater. Res. Innovations* **2002**, *6*, 128–140.

- (29) Voiry, D.; Yang, J.; Kupferberg, J.; Fullon, R.; Lee, C.; Jeong, H. Y.; Shin, H. S.; Chhowalla, M. High-Quality Graphene Via Microwave Reduction Of Solution-Exfoliated Graphene Oxide. *Science* **2016**, *353*, 1413–1416.
- (30) de la Hoz, A.; Díaz-Ortiz, Á.; Moreno, A. Microwaves In Organic Synthesis. Thermal And Non-Thermal Microwave Effects. *Chem. Soc.* **2005**, *34*, 164–178.
- (31) Kappe, C. O. Controlled Microwave Heating in Modern Organic Synthesis. *Angew. Chem., Int. Ed.* **2004**, *43*, 6250–6284.
- (32) Malhotra, A.; Vashaee, D. Simultaneous Rapid Sintering and Solid-State Reaction Using Microwave Radiation Workshop on Electromagnetic Effects in Materials Synthesis; Carnegie Mellon University: Pittsburgh, PA, USA, 2017, 5.
- (33) Gedye, R.; Smith, F.; Westaway, K.; Ali, H.; Baldisera, L.; Laberge, L.; Rousell, J. The Use Of Microwave Ovens For Rapid Organic Synthesis. *Tetrahedron Lett.* **1986**, *27*, 279.
- (34) Gracia, J.; Escuin, M.; Mallada, R.; Navascues, N.; Santamaria, J. Nano-Heaters: New Insights On The Outstanding Deposition Of Dielectric Energy On Perovskite Nanoparticles. *Nano Energy* **2016**, 20, 20–28.
- (35) Hall, M., Nozariasbmarz, A., Vashaee, D. Decrystallization and Microstructure Modification Using Microwave Processing Workshop on Electromagnetic Effects in Materials Synthesis, Carnegie Mellon University, Pittsburgh, PA, USA, 5, 6 June (2017).
- (36) Vashaee, D., Hall, M., Malhotra, A., Nozari, A., In-Situ Sintering Field Induced Decrystallization of Thermoelectric Materials Workshop on Electromagnetic Effects in Materials Synthesis, Carnegie Mellon University, Pittsburgh, PA, USA, 5, (2017). Nozariasbmarz, A.; Collins, H.; Dsouza, K.; Polash, M. H.; Hosseini, M.; Hyland, M.; Liu, J.; Malhotra, A.; Ortiz, F. M.; Mohaddes, F.; Ramesh, V. P.; Sargolzaeiaval, Y.; Snouwaert, N.; Özturk, M. C.; Vashaee, D. Review Of Wearable Thermoelectric Energy Harvesting: From Body Temperature To Electronic Systems. Appl. Energy 2019, 114069.
- (37) Kocevski, V.; Wolverton, C. Designing High-Efficiency Nanostructured Two-Phase Heusler Thermoelectrics. *Chem. Mater.* **2017**, 29, 9386–9398.
- (38) Yan, X.; Joshi, G.; Liu, W.; Lan, Y.; Wang, H.; Lee, S.; Simonson, J. W.; Poon, S. J.; Tritt, T. M.; Chen, G.; Ren, Z. F. Enhanced Thermoelectric Figure Of Merit Of P-Type Half-Heuslers. *Nano Lett.* **2010**, *11*, 556–560.
- (39) Anirudha, K.; Nagini, M.; Ghosh, S.; Shabadi, R.; Pradeep, K. G.; Mallik, R. C.; Murty, B. S.; Varadaraju, U. V. Ti₂Nicosnsb-A New Half-Heusler Type High-Entropy Alloy Showing Simultaneous Increase In Seebeck Coefficient And Electrical Conductivity For Thermoelectric. *Appl. Sci. Rep.* **2019**, *9*, 5331.
- (40) Xie, H.; Wang, H.; Fu, C.; Liu, Y.; Snyder, G. J.; Zhao, X.; Zhu, T. The Intrinsic Disorder Related Alloy Scattering In Zrnisn Half-Heusler Thermoelectric Materials. *Sci. Rep.* **2014**, *4*, 6888.
- (41) Zaferani, S. H.; Ghomashchi, R.; Vashaee, D. Strategies For Engineering Phonon Transport In Heusler Thermoelectric Compounds. *Renewable Sustainable Energy Rev.* **2019**, *112*, 158–169.
- (42) Poudel, B.; Hao, Q.; Ma, Y.; Lan, Y.; Minnich, A.; Yu, B.; Yan, X.; Wang, D.; Muto, A.; Vashaee, D.; Chen, X.; Liu, J.; Dresselhaus, M. S.; Chen, G.; Ren, Z. High-Thermoelectric Performance of Nanostructured Bismuth Antimony Telluride Bulk Alloys. *Science* 2008, 320, 634–638.
- (43) Nozariasbmarz, A.; Hosseini, M.; Vashaee, D. Interfacial ponderomotive force in solids leads to field induced dissolution of materials and formation of non-equilibrium nanocomposites. *Acta Mater.* **2019**, *179*, 85–92.
- (44) Nozariasbmarz, A.; Krasinski, J. S.; Vashaee, D. N-Type Bismuth Telluride Nanocomposite Materials Optimization for Thermoelectric Generators in Wearable Applications. *Materials* **2019**, *12*, 1529.
- (45) Norouzzadeh, P.; Ede, K. F.; Vashaee, D. The effect of nanostructuring on the spectral population of electrons and phonons. *J. Alloys Compd.* **2018**, 753, 234–238.

- (46) Vashaee, D.; Zhang, Y.; Shakouri, A.; Zeng, G.; Chiu, Y. J. Cross-Plane Seebeck Coefficient In Superlattice Structures In The Miniband Conduction Regime. *Phys. Rev. B* **2006**, *74*, 195315.
- (47) Satyala, N.; Tahmasbi Rad, A.; Zamanipour, Z.; Norouzzadeh, P.; Krasinski, J. S.; Tayebi, L.; Vashaee, D. Reduction Of Thermal Conductivity Of Bulk Nanostructured Bismuth Telluride Composites Embedded With Silicon Nano-Inclusions. *J. Appl. Phys.* **2014**, *115*, No. 044304.
- (48) Satyala, N.; Norouzzadeh, P.; Vashaee, D. Nano Bulk Thermoelectrics: Concepts, Techniques, And Modeling In Nanoscale Thermoelectrics; Springer: Cham. 2014, pp. 141–183.
- (49) Norouzzadeh, P.; Zamanipour, Z.; Krasinski, J. S.; Vashaee, D. The Effect Of Nanostructuring On Thermoelectric Transport Properties Of P-Type Higher Manganese Silicide Mnsi1. 73. *J. Appl. Phys.* **2012**, *112*, 124308.
- (50) Kang, S. J. L Sintering: Densification, Grain Growth And Microstructure Elsevier (2004).
- (51) Mastrovito, C.; Lekse, J. W.; Aitken, J. A. Rapid Solid-State Synthesis Of Binary Group 15 Chalcogenides Using Microwave Irradiation. *J. Solid State Chem.* **2007**, *180*, 3262–3270.
- (52) Birkel, C. S.; Zeier, W. G.; Douglas, J. E.; Lettiere, B. R.; Mills, C. E.; Seward, G.; Birkel, A.; Snedaker, M. L.; Zhang, Y.; Snyder, G. J.; Pollock, T. M.; Seshadri, R.; Stucky, G. D. Rapid Microwave Preparation Of Thermoelectric Tinisn And Ticosb Half-Heusler Compounds. *Chem. Mater.* **2012**, *24*, 2558–2565.
- (53) Yang, F.; Fan, X. A.; Rong, Z. Z.; Cai, X. Z.; Li, G. Q. Lattice Thermal Conductivity Reduction Due to In Situ-Generated Nano-Phase in Bi0.4Sb1.6Te3 Alloys by Microwave-Activated Hot Pressing. *J. Electron. Mater.* **2014**, 43, 4327.
- (54) Waldow, P.; Wolff, I. The skin-effect at high frequencies. *IEEE Trans. Microwave Theory Tech.* **1985**, 33, 1076–1082.
- (55) Wu, E. J.; Ceder, G. Computational investigation of dielectric absorption at microwave frequencies in binary oxides. *J. Appl. Phys.* **2001**, *89*, 5630–5636.
- (56) Adams, J. Electromagnetic Theory (IEEE Press Series on Electromagnetic Wave Theory); McGraw-Hill 2007.
- (57) Orfanidis, S. J. Electromagnetic waves and antennas; Rutgers University New Brunswick 2002.
- (58) Morales, G. J.; Lee, Y. C. Ponderomotive-Force Effects In A Nonuniform Plasma. *Phys. Rev. Lett.* **1974**, 33, 1016.
- (59) Rybakov, K. I.; Semenov, V. E.; Link, G.; Thumm, M. Preferred Orientation Of Pores In Ceramics Under Heating By A Linearly Polarized Microwave Field. *J. Appl. Phys.* **2007**, *101*, 084915.
- (60) Rybakov, K. I.; Olevsky, E. A.; Semenov, V. E. The Microwave Ponderomotive Effect On Ceramic Sintering. *Scr. Mater.* **2012**, *66*, 1049–1052.
- (61) Get'man, O. I.; Panichkina, V. V.; Paritskaya, L. N.; Skorokhod, V. V.; Samelyuk, A. V.; Bykov, Y. V.; Eremeev, A. G. Effect of microwave heating on the mass transfer, phase formation, and microstructural transformations in the Y₂O₃-Al₂O₃ diffusion couple. *Powder Metall. Met. Ceram.* **2014**, *53*, 8–18.
- (62) Get'man, O. I.; Panichkina, V. V.; Paritskaya, L. N.; Radchenko, P. Y.; Samelyuk, A. V.; Skorokhod, V. V.; Bykov, Y. V.; Eremeev, A. G. Interdiffusion and structural changes in the $Cr_2O_2-Al_2O_3(ZrO_2)$ diffusion couple under microwave heating. *Powder Metall. Met. Ceram.* **2013**, *51*, 666–676.
- (63) Chen, C. S. Effect of dopant valence state of Mn-ions on the microstructures and nonlinear properties of microwave sintered ZnO-V 2 O 5 Varistors. *J. Mater. Sci.* **2003**, 38, 1033–1038.
- (64) Rybakov, K. I.; Semenov, V. E.; Egorov, S. V.; Eremeev, A. G.; Plotnikov, I. V.; Bykov, Y. V. Microwave heating of conductive powder materials. *J. Appl. Phys.* **2006**, *99*, No. 023506.
- (65) Whittaker, A. G. Diffusion in microwave-heated ceramics. *Chem. Mater.* **2005**, *17*, 3426–3432.
- (66) Booske, J. H.; Cooper, R. F.; Freeman, S. A.; Rybakov, K. I.; Semenov, V. E. Microwave Ponderomotive Forces In Solid-State Ionic Plasmas. *Phys. Plasmas* **1998**, *5*, 1664–1670.

- (67) Nozariasbmarz, A. In-situ Sintering Decrystallization of Thermoelectric Materials using Microwave Radiation. PhD Dissertation, North Carolina State University 2017.
- (68) Malhotra, A. Thermoelectric Generators for Wearable Application: Materials and Devices; PhD Dissertation, North Carolina State University 2019.
- (69) Rowe, D. M. CRCHandbook Of Thermoelectricity; CRC press, 1995.
- (70) Xie, W.; Populoh, S.; Gałązka, K.; Xiao, X.; Sagarna, L.; Liu, Y.; Trottmann, M.; He, J.; Weidenkaff, A. Thermoelectric Study Of Crossroads Material MnTe Via Sulfur Doping. *J. Appl. Phys.* **2014**, *115*, 103707.
- (71) Zheng, Y.; Lu, T.; Polash, M. M. M.; Rasoulianboroujeni, M.; Liu, N.; Manley, M. E.; Deng, Y.; Sun, P. J.; Chen, X. L.; Hermann, R. P.; Vashaee, D.; Heremans, J. P.; Zhao, H. Paramagnon Drag In High Thermoelectric Figure Of Merit Li-Doped MnTe. *Sci. Adv.* **2019**, *5*, eaat9461.

NOTE ADDED AFTER ASAP PUBLICATION

This paper published ASAP on October 22, 2020 with an error due to production in the first column of Table 1. A new version was reposted on October 23, 2020.